applied sciences

MDPI

Article

Comparison of Single and Dual Coherent Blades for a Vertical Axis Carousel Wind Rotor Using CFD and Wind Tunnel Testing

Marcin Augustyn and **Filip Lisowski** *

Department of Machine Design and Composite Structures, Faculty of Mechanical Engineering, Cracow University of Technology, Al. Jana Pawła II 37, 31-864 Kraków, Poland; marcin.augustyn@pk.edu.pl
* Correspondence: filip.lisowski@pk.edu.pl

Abstract: This paper focused on the investigation of the blades for a carousel rotor of a wind turbine with a vertical axis. Cross sections of the single coherent (SC) and the dual coherent (DC) blades were compared in terms of the aerodynamic forces and aerodynamic torque generated during rotor operation for various wind attack angles. The design of the DC blade is novelty proposed by the authors. The main objective of the study was to determine the influence of the blade cross-section on the propelling torque of a wind turbine with three blades, which is an important parameter for rotor starting. First, experimental studies were carried out in a wind tunnel for real-size blade models. A CFD analysis of the airflow around the blades was then conducted. The obtained results were used to evaluate the suitability of applying the studied blade types in the design of the carousel wind rotor. The assessment compared the drag force and the lift force as well as aerodynamic torque as a function of a wind attack angle. It was concluded that the rotor with three DC blades involved mainly the drag force in contrast to the rotor with three SC blades that also involved the lift force to a greater extent. Despite the rotor with DC blades obtained greater values of the drag forces on the blades, the rotor with SC blades obtained a greater starting torque.

Keywords: CFD simulation; wind tunnel testing; blade cross-section

check for updates

Citation: Augustyn, M.; Lisowski, F. Comparison of Single and Dual Coherent Blades for a Vertical Axis Carousel Wind Rotor Using CFD and Wind Tunnel Testing. *Appl. Sci.* **2023**, *13*, 12624. https://doi.org/10.3390/app132312624

Academic Editor: Ricardo Castedo

Received: 26 October 2023
Revised: 16 November 2023
Accepted: 21 November 2023
Published: 23 November 2023

1. Introduction

The wind energy required to power wind turbines is currently considered a renewable energy source that is completely free and inexhaustible. It is widely available, therefore delivering it to wind turbines does not require arranging a supply chain, as is the case with fossil fuels. The generation of wind energy does not release harmful carbon dioxide, sulfur oxides, or other pollutants into the atmosphere. It is a pure and cheap source of energy that, thanks to its virtually global reach, helps remote or hard-to-reach populations to access electricity. Nowadays, the share of renewable energy in the fuel market, especially wind and solar energies, continues to grow strongly. According to statistical data [1], renewable energy accounted for 13% of the total global power generation in 2022. On the other hand, in 2021 it grew by 17% and accounted for more than half of the increase in global electricity production over the past two years. Comparing the contribution of wind power capacity to the overall electric power produced in a country or region, the same report referred to 2021 indicates the following shares: 47.8% in Asia Pacific with 39.9% in China, 28.2% in Europe, 18.8% in total North America, and 13.1% in the rest of the world.

Wind turbines with horizontal axis (HAWTs) [2,3] are currently the most popular wind turbine design. Rotors with a horizontal axis convert the kinetic energy of the wind into mechanical work, using part of the power of the air stream to drive various types of machines and devices. If the powered machine is an electric generator, then the wind turbine or several wind turbines grouped together are called a wind power plant. Nowadays, the most technologically advanced wind turbines are those with a nacelle containing a rotor consisting of blades mounted radially in a hub, a gearbox and a shaft housed on bearings and connected to a generator. The nacelle is mounted pivotally on a tower or mast, along with a device to control the speed of the rotor, as well as a self-adjusting system for wind direction. The blades set on the shaft drive the wind turbine generator, and the gearbox regulates the speed of the generator depending on the speed of the rotor, which movement is forced by the wind force. Therefore, the efficiency of the rotor is mainly related to the shape of the blades [4]. The most common solution of HAWTs, for both high, medium, and low power, is the three-bladed rotor design with airfoil-shaped cross sections, as shown in Figure 1a.

(**a**) (**b**)

Figure 1. Basic types of wind turbines: (**a**) the HAWT turbine; (**b**) the VAWT turbine.

This shape provides the rotor blades with adequate aerodynamic properties and is directly related to the lifting force that is created when the pressure on the lower part of the airfoil is greater than on the upper part. In general, the wind rotors' aerodynamic efficiency is mainly affected by the shape of the blades and the speed ratio Z given by the following equation:

$$Z = \frac{\omega R}{W} \tag{1}$$

where ω stands for the rotor angular velocity [rad/s], R is the rotor radius [m], and W stands for the wind speed [m/s]. HAWTs are high-speed turbines, which require the use of additional mechanisms to protect against reaching critical rotor speed. For example, the rotor axis or the blades change the angular position depending on the wind speed to reduce the drag force. The three-blade HAWT achieves the best use of the energy of the air stream, making this type the most popular [5].

The rapid development and great success of wind turbines with horizontal axis in the wind power industry has also contributed to the increasing development of wind turbines with vertical axis (VAWTs) [6]. An example of the VAWT turbine is shown in Figure 1b. Despite higher wind power utilization rate, wind turbines with vertical axis represent a minor share of installations in operation today. The reason for less interest in this type of structure is mainly the load occurring during rotor rotation. The vertical axis of the rotor is subjected to periodic bending that changes over time. The frequency of changes in the load on the vertical axis of the rotor results from its rotation frequency. In the field of external forces resulting from the influence of wind and gravity, gyroscopic effects are created and, as a result, the rotor rotation axis cannot reach the position of dynamic equilibrium [7]. Vertical axis wind turbines are not as expensive to build and operate as horizontal axis wind turbines. Despite this, they have not become that common, mostly because of the limited speed and their low efficiency [8,9]. The three basic designs of VAWT are: Darrieus, Savonius, and H-type rotors [10–12]. The Darrieus rotor patented in 1931 has two thin arc-shaped blades that rotate around the vertical axis. The rotor design is simple, but with a low starting torque. It was modified several times in the following years, including the use of an additional rotor as a starting motor [13]. The authors of Ref. [14] proposed a Darrieus multi-turbine system in which the coupled rotors meshed with each other. The authors found that such an arrangement improved the efficiency of a single rotor. An overview of the Darrieus rotors development and their applications was described in Ref. [15]. In turn, the authors of Refs. [16,17] focused on practical applications of the Darrieus rotor, which was the application of such a rotor in wind or hydro microgenerator.

The starting torque of the Darrieus rotor is practically zero, therefore an additional drive is required for starting [18,19]. As an auxiliary drive for starting the Darrieus rotor, an electric motor or a secondary rotor of a different design that provides high starting torque, such as the Savonius rotor, can be used. This rotor consists of two curved blades arranged in a S-shape. There is usually a gap between the blades of 10% to 15% of the rotor blade diameter [20]. Refs. [21–23] present research on how to obtain a more uniform static torque coefficient or the possibility of improving the power factor with respect to the basic Savonius rotor or its improved forms.

Combining the structural and aerodynamic advantages of several different turbines, the other modified designs of wind turbines can be obtained. For example, the TURBY's turbine [24], which is a modification of the Darrieus turbine and is designed for operation on the roof of a building. Blades of the rotor, which are mounted obliquely, make it possible to use the energy of wind acting both horizontally and at different angles. Other examples are the H-Darrieus turbine [25] or the spiral wind turbine [26]. These designs provide uniform operation for any wind direction and are quiet. One of the main advantages of VAWTs is that there is no need to use a wind direction adjustment system, and the design of the rotors and the mechanical and electrical equipment used in these turbines is less complex than for HAWTs.

1.1. A Carousel Wind Rotor Design

An alternative to the above designs of vertical axis wind rotors is the carousel wind rotor presented by Ryś in study [27]. The kinematic diagram and cross-sectional view of this rotor is presented in Figures 2 and 3. A planetary gear is the main component of the carousel wind rotor, which is connected with the vertical drive shaft and three blades. The blades should be properly balanced to minimize the resistance on the bearings during operation. Their planetary motion is synchronized by a gearbox with a gear ratio of 1:2. The blades rotate at half speed and in the opposite direction to the direction of rotor rotation. A self-adjusting system determines the angular orientation of the rotor with respect to the wind direction. The self-adjusting system is directly coupled to a worm gear located under the rotor housing. The gear ratio causes the blade surfaces to work alternately. Therefore, the blade profile must have point symmetry. One of the typical features of the carousel wind rotor is the large starting torque, which is forced mainly by the drag force, and less by the lifting force acting on the blades. Another characteristic feature of the carousel rotor is the low speed of the turbine. Due to the kinematics of the gearbox, the rotor reaches and maintains maximum speed despite the increasing wind speed. The kinematic diagram of the carousel wind rotor is shown in Figure 2a, whereas its cross-sectional view is shown in Figure 2b. The carousel wind rotor consists of: at least three blades (7) mounted on vertical pins (10) and coupled with gears z2; a rotor mast (9); a rotor (1) coupled to the drive shaft (5) and rotating relative to a stationary housing (2); a sleeve (4) mounted in the housing with a bearing; the blades axles (6); the planetary gearbox (8) with a gear ratio (z1/z2) of 1:2; and a worm gear (3) to attach the self-adjusting system to the wind direction. A full-scale physical model of a carousel wind rotor built to verify the movement of the blades, positioned by a planetary gear, is shown in Figure 3.

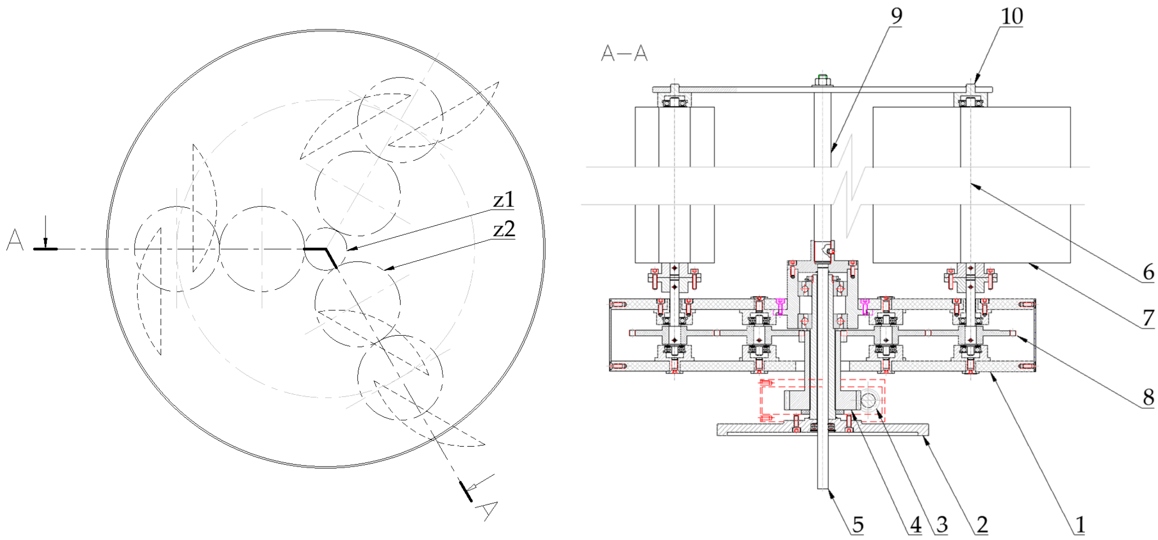

(**a**) (**b**)

Figure 2. Vertical axis carousel wind rotor: (**a**) kinematic diagram; (**b**) cross-sectional view.

(**a**) (**b**)

Figure 3. Physical model of a carousel wind rotor: (**a**) front view; (**b**) isometric view.

The gear ratio determining the position of the blades during operation and the profile of the blades are of great importance in determining the most favorable design parameters of the carousel wind rotor. A gear ratio of 1:2 was assumed in this study, and the main focus was on the comparison of blades with single and dual coherent cross-sections.

1.2. Movement of a Carousel Wind Rotor Blade

Diagrams presenting the movement and external forces associated with a single blade, using a dual coherent cross-section as an example, are shown in Figure 4a,b. When considering the SC blade, the angular positions for each step are analogous. The x, y coordinate system is a global coordinate system with the origin corresponding to the rotor's axis of rotation. In turn, the η, ξ movable coordinate system is related to the blade. The forces P_x, P_y and moment M_z, shown in Figure 4b, are related to the x, y coordinates. The magnitude of these three loads is directly influenced by the wind speed W. The change in wind direction is determined by two angles: β, which is the angle describing the action of the wind relative to the rotor, and γ, which is the angle of the wind attack on a single blade ($\gamma = \alpha/2$).

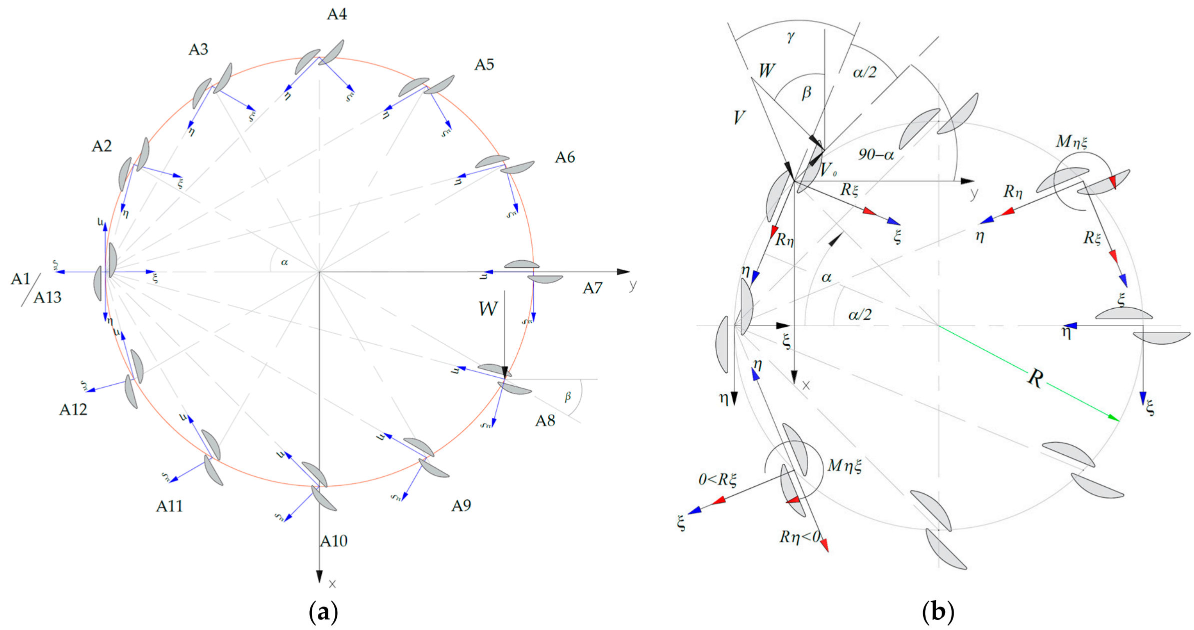

Figure 4. The movement of the carousel rotor blade: (**a**) positions of the single blade (α = 22.5°); (**b**) forces acting on the rotor blade for subsequent angular positions.

During turbine operation, the blades move around the rotor axis under the action of the wind. The planetary gear determines the angular position of the blades. The appropriate planetary gear ratio should be selected to provide the most advantageous blade position relative to the wind direction. The most preferred position for easy rotor starting is A7, for which β = 0. The range of angular positions between A4 and A10 provide effective operation of the blade. In contrast, the range of angular positions between A10 and A4 results in low aerodynamic drag even though the blade passes upwind. The planetary motion of the blade, forced by a gearbox with a ratio of 1:2, causes the blade cross-section to rotate by 180° during a single cycle of the blade. The single cycle is a movement around the rotor axis starting at position A1 and returning again to position A13. In consequence, the blade reaches the starting position every second cycle.

2. Materials and Methods

2.1. Carousel Wind Rotor Blade Profiles

Considering the principles of the of the blade motion, presented in the introduction, the blade cross-section must have point symmetry. In this study, we compared two different blade cross-sections. The first one, known as the single coherent, is shown in Figure 5. The outline of the blade is shaped with a flat surface on the first half of the blade parallel to the blade chord, and on the second half it curves outward along an arc and turns into a convex surface. The opposite surface the blade has an identical shape, rotated by 180°, resulting in point symmetry. The second cross-section of the blade, proposed by the authors, is defined as the dual coherent (Figure 6). The blade consists of two identical lobes placed in point symmetry relative to each other. The axis of the blade's rotation coincides with the symmetry point. The inner surface of a single lobe is parallel to a blade chord. It is also flat, while the outer surface is convex. The cross-section of the dual coherent blade is a modification of the cross-section of single coherent blade introducing a gap between the lobes.

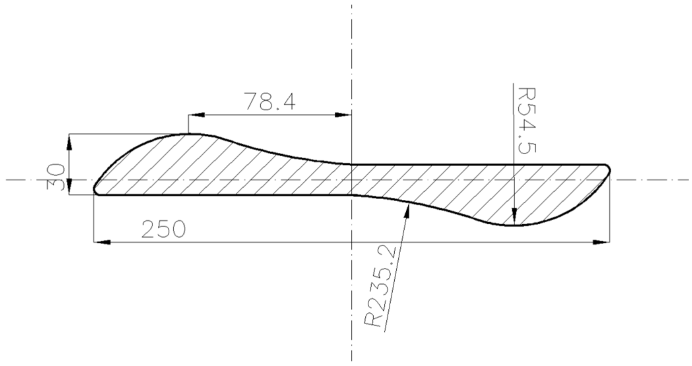

Figure 5. Profiles of the single coherent blade with dimensions in mm.

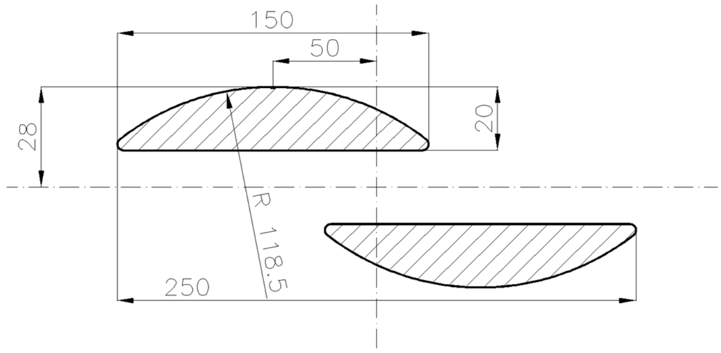

Figure 6. Profiles of the dual coherent blade with dimensions in mm.

Comparing structural integrity, the DC blade can achieve higher stiffness due to the greater distance between supporting elements within its structure. The DC blade can also be easier in manufacturing due to the less complex cross section of the single profile. The main dimensions of the tested blades were summarized in Table 1.

Table 1. Main dimensions of the tested blade models.

Dimension [m]	Single Coherent Blade	Dual Coherent Blade
Blade width	$a_S = 0.250$	$a_T = 0.250$
Blade length	$b_S = 0.044$	$b_T = 0.076$
Blade height	$h = 0.625$	$h = 0.625$
Gap between the lobes	-	$b_{Tg} = 0.016$

The geometric scale of the tested blade was 1:1. Therefore, it was not necessary to specify other similarity criteria. Aerodynamic tests of single coherent and dual coherent blades were carried out to determine aerodynamic forces, aerodynamic torque, and next to calculate the propelling torque of the wind turbine rotor. For this purpose, the rigid full-scale blades models were prepared as shown in Figure 7.

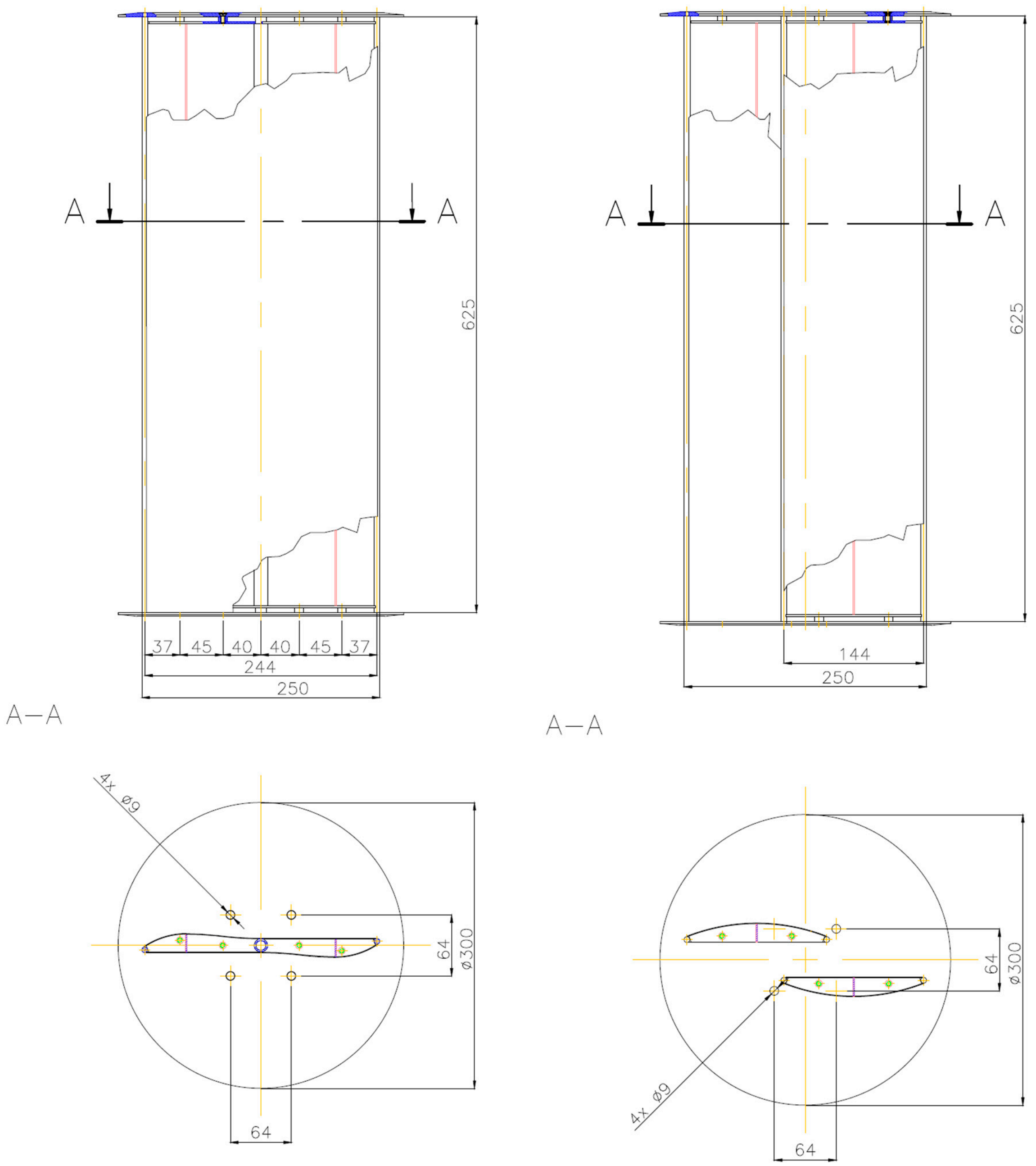

(**a**) (**b**)

Figure 7. Front views and cross-section of the full-scale blades models with dimensions in mm: (**a**) the SC blade; (**b**) the DC blade.

2.2. Experiments in the Wind Tunnel

Tests in a wind tunnel were carried out at the Wind Engineering Laboratory of the Cracow University of Technology [28]. The tunnel operated in a closed circuit. A fan that sucked the air was located behind the measuring section. The air returned to the initial part of the measuring space through the return duct. The main dimensions of the wind tunnel working section are: 2.20 m wide, 1.40 m high, and 10.00 m long. The first part of the 6 m long working section is used to form the wind speed profile and generate turbulence. Turbulent air flow is created using turbulence generators, such as barriers and spiers with appropriate geometry and shapes, as shown in Figure 8.

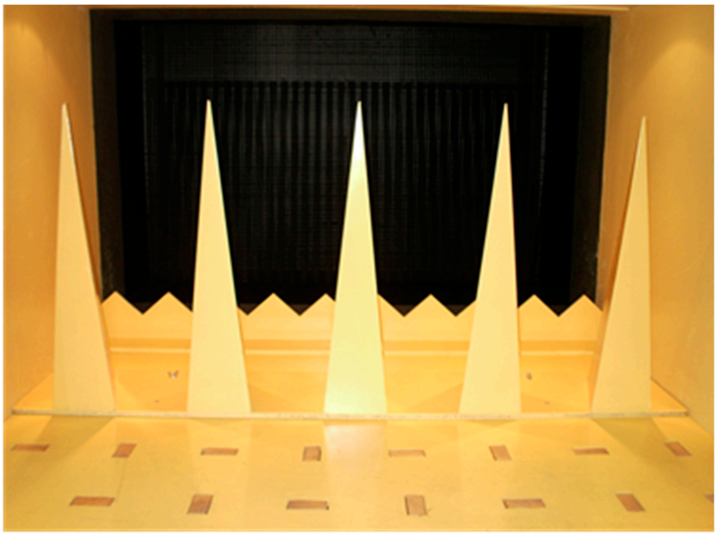

Figure 8. Spires and a barrier to generate turbulent flow in the wind tunnel measuring section.

The wind profile was determined starting from a height of 300 mm above the upper surface of the measuring table. At this height, the tested blade was attached to a strain gauge aerodynamic balance. The part connecting the blade with the aerodynamic balance was covered by a fairing. The profile of the wind and the intensity of turbulence are presented in Figure 9a,b.

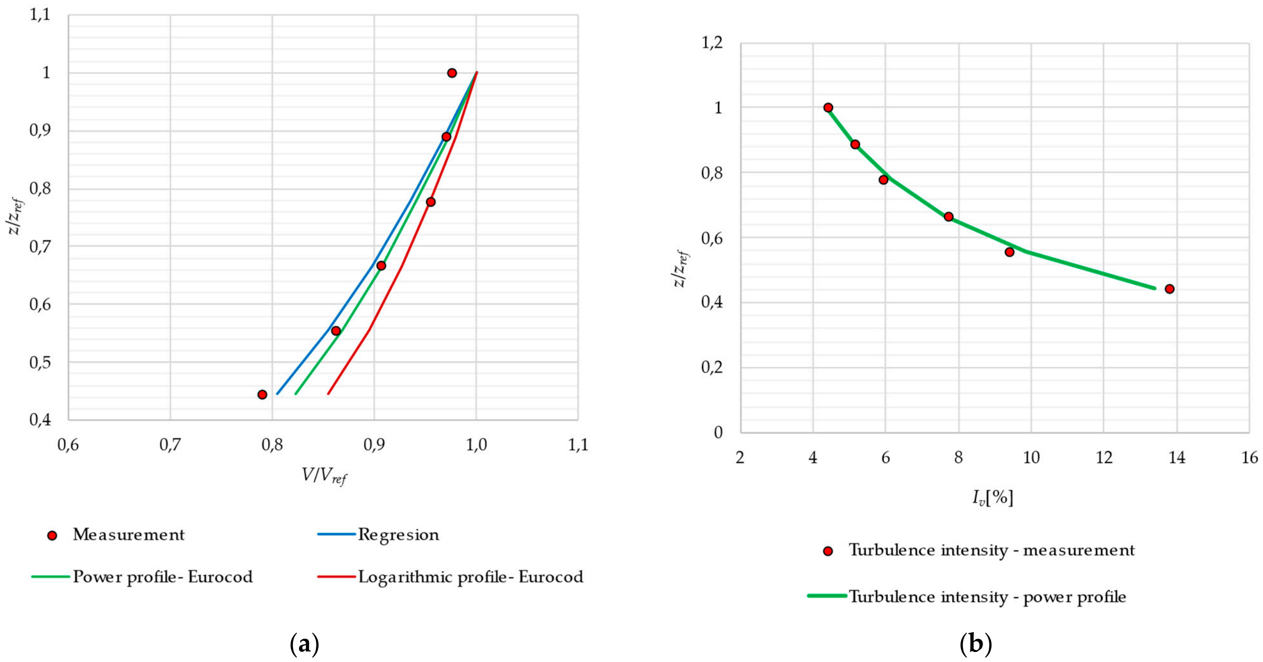

Figure 9. (**a**) Wind speed profile; (**b**) turbulence intensity.

According to standard [29], the profiles of the wind were described by the power law formula:

$$\frac{V(z)}{V_{ref}} = \left(\frac{z}{z_{ref}}\right)^{\alpha} \quad (2)$$

where V_{ref}—the reference velocity at a reference height z_{ref}; α—the power low exponent i.e., the coefficient of roughness, z—the height, and V—the average wind speed.

Turbulence intensities $I_V(z)$ were calculated according to the formula:

$$I_V(z) = \frac{\sigma(z)}{V(z)} \tag{3}$$

where $\sigma(z)$—standard deviations.

The speed of the wind was calculated based on the pressure measurements, which were carried out using a set of differential pressure sensors with pitot tubes. The pressure sensors were located in a vertical plane, as shown in Figure 10a,b, on the left side of the blade under test. A measurement time of 10 s was assumed. During that time 6000 samples were collected. The average wind speed was calculated based on the average wind profile values for all test cases. The profile of the wind was determined in the height range from 300 mm to 900 mm with a step of 100 mm. The main parameters of the measurements were summarized in Table 2.

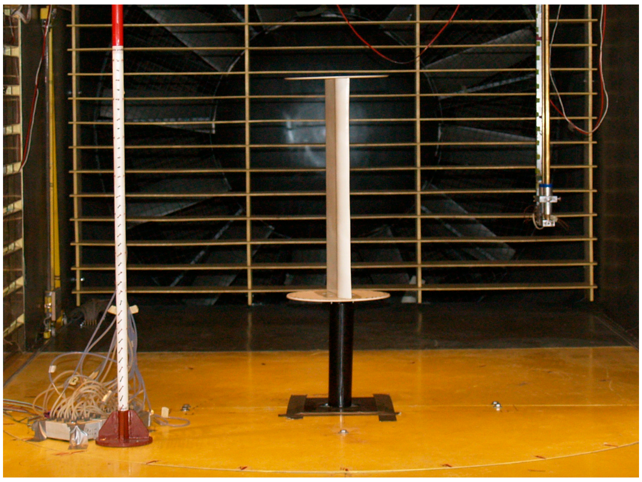

(**a**)

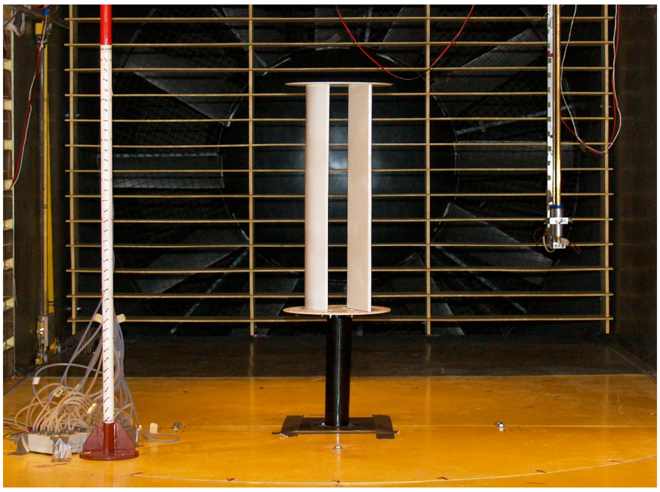

(**b**)

Figure 10. The blade models during tests in the wind tunnel: (**a**) the SC blade; (**b**) the DC blade.

Table 2. The main parameters of the measurements.

Parameter	Value
Geometric scale k_D	1:1
Average speed of the wind W [m/s]	12.5
Mean turbulence intensity of the wind velocity I_V [%]	8
Number of considered directions of the wind action	18 (0–180°)
Reference pressure measurement	7 points along the blade height

A five-component strain gauge balance was installed under the floor of the working section of the wind tunnel. These five components represent aerodynamic forces P_x, P_y, aerodynamic torque M_{xy}, and aerodynamic moments M_x, M_y. A diagram of the measurement system used in the study is shown in Figure 11. The model of the examined blade was installed on the strain gauge balance. The aerodynamic balance was connected to an amplifier, which included data acquisition systems for collecting records of measured aerodynamic forces and moments. The aerodynamic balance was used to determine three components P_x, P_y, and M_{xy} referred to the x,y coordinates presented in Figure 11. The wind angle was changed using a turntable actuated by an electric motor. The turntable is a coaxial part of the aerodynamic balance. A stepper motor, controlled by the stepper motor control system, caused the model to rotate, which simulated changes in the angle of the wind attack. Sensors for measuring pressure, arranged in the vertical plane, were connected with the pressure scanner. Pressure sensors were used to determine the wind profile. All experimental data were collected using a data acquisition card connected to a computer.

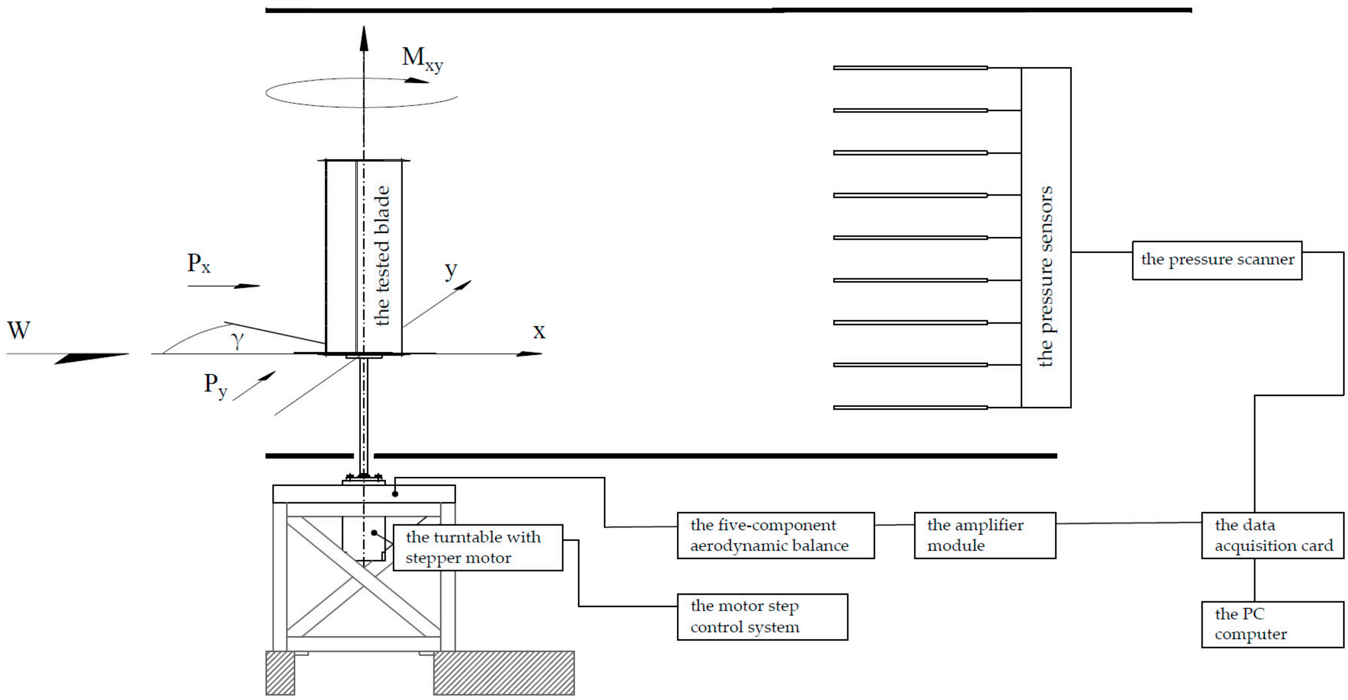

Figure 11. Diagram of the measurement system.

2.3. CFD Analysis

Both single coherent and dual coherent blades under consideration were also examined numerically with computational fluid dynamic analysis using ANSYS/Fluent Release 2022 R2 software. For both types of blades, sets of two-dimensional discrete models were prepared for the angle of the wind attack from 0° to 180° every 10°. The analysis included boundary layer modeling and mesh validation.

2.3.1. Governing Equations and Turbulence Model

Mass and momentum conservation Equations (4) and (5) are solved for all flows analyzed in ANSYS Fluent [30]. The additional equation of energy conservation is solved for analysis involving heat transfer or fluid compressibility. Because neither of these effects were present in our analysis, the energy equation was not included.

$$\frac{\partial \rho}{\partial t} + \nabla \times \left(\rho \vec{v}\right) = S_m \tag{4}$$

$$\frac{\partial}{\partial t}\left(\rho \vec{v}\right) + \vec{v} \times \nabla\left(\rho \vec{v}\right) = -\nabla p + \nabla \times \left(\bar{\bar{\tau}}\right) + \rho \vec{g} + \vec{F} \tag{5}$$

where ρ—the fluid density; ∇—Nabla operator; $\vec{v}$—velocity vector; S_m—mass from the dispersed phase, e.g., from the evaporation of liquid droplets, added to the continuous phase; p—the static pressure; $\rho \vec{g}$—the gravitational body force; $\vec{F}$—body force; $\bar{\bar{\tau}}$—stress tensor given by Equation (6).

$$\bar{\bar{\tau}} = \mu\left[\left(\nabla \vec{v} + \nabla \vec{v}^{T}\right) - \frac{2}{3}\nabla \times \vec{v} I\right] \tag{6}$$

where μ—molecular viscosity; I—unit tensor.

The shear stress transport model (k-ω SST) was used in the calculations. This two-equation turbulence model was developed by Menter [31,32] to effectively blend the k-ω

Wilcox model [33] near walls and standard k-ε model [34] in the fare field. The blending functions were developed to activate particular model depending on flow regions. This makes the k-ω SST model more accurate and reliable for a wide range of flows than standard k-ω or k-ε models [35]. The k-ω SST model is widely used in the analysis of airfoils or wind turbine blades [36–38]. The turbulence kinetic energy k and the specific dissipation rate ω are obtained from the transport Equations (7) and (8).

$$\frac{\partial}{\partial t}(\rho k) + \frac{\partial}{\partial x_i}(\rho k u_i) = \frac{\partial}{\partial x_i}\left(\Gamma_k \frac{\partial k}{\partial x_j}\right) + \widetilde{G}_k - Y_k + S_k \tag{7}$$

$$\frac{\partial}{\partial t}(\rho \omega) + \frac{\partial}{\partial x_j}(\rho \omega u_i) = \frac{\partial}{\partial x_j}\left(\Gamma_\omega \frac{\partial \omega}{\partial x_j}\right) + G_\omega - Y_\omega + D_\omega + S_\omega \tag{8}$$

where $\widetilde{G}_k$—the turbulence kinetic energy generation caused by the average velocity gradients; G_ω—the generation of ω; Y_k and Y_ω—the dissipation of k and ω due to turbulence; D_ω—the cross-diffusion term; S_k and S_ω—user-define source terms; Γ_k and Γ_ω—the effective diffusivity of k and ω given by Equations (9) and (10).

$$\Gamma_k = \mu + \frac{\mu_t}{\sigma_k} \tag{9}$$

$$\Gamma_\omega = \mu + \frac{\mu_t}{\sigma_\omega} \tag{10}$$

where μ_t—the turbulent viscosity given by Equation (11), whereas σ_k and σ_ω—the turbulent Prandtl numbers for k and ω given by Equations (12) and (13)

$$\mu_t = \frac{\rho k}{\omega} \frac{1}{max\left[\frac{1}{\alpha^*}, \frac{SF_2}{a_1 \omega}\right]} \tag{11}$$

$$\sigma_k = \frac{1}{F_1/\sigma_{k,1} + (1 - F_1)/\sigma_{k,2}} \tag{12}$$

$$\sigma_\omega = \frac{1}{F_1/\sigma_{\omega,1} + (1 - F_1)/\sigma_{\omega,2}} \tag{13}$$

where S—the magnitude of strain rate; α^*—the coefficient of damping the turbulent viscosity causing a low-Reynolds-number correction; F_1 and F_2—blending functions given by the following equations:

$$F_1 = \tanh\left(\phi_1^4\right) \tag{14}$$

$$\phi_1 = min\left[max\left(\frac{\sqrt{k}}{0.09\omega y'}, \frac{500\mu}{\rho y^2 \omega}\right), \frac{4\rho k}{\sigma_{\omega,2} D_\omega^+ y^2}\right] \tag{15}$$

$$D_\omega^+ = max\left(2\rho \frac{1}{\sigma_{\omega 2}} \frac{1}{\omega} \frac{\partial \mathrm{k}}{\partial x_j} \frac{\partial \omega}{\partial x_j}, 10^{-10}\right) \tag{16}$$

$$F_2 = \tanh\left(\phi_2^2\right) \tag{17}$$

$$\phi_2 = max\left(\frac{2\sqrt{k}}{0.09\omega y'}, \frac{500\mu}{\rho y^2 \omega}\right) \tag{18}$$

where y—the distance from the field point to the nearest surface; D_ω^+—the positive cross-diffusion term. The constant parameters accepted by ANSYS Fluent [39] are: $\sigma_{k,1}$ = 1.176, $\sigma_{\omega,1}$ = 2.0, $\sigma_{k,2}$ = 1.0, $\sigma_{\omega,2}$ = 1.168, α_1 = 0.31.

2.3.2. Mesh and Boundary Conditions

Physical models of the blade prepared for wind tunnel testing were equipped with flat, round plates to eliminate the edge effects. Thanks to this, the air flow problem was reduced to a two-dimensional problem. Therefore, two-dimensional discrete blade models were accepted for CFD. For each type of blade, 19 discrete models were prepared, differing in the angular position of the blade, and thus the wind angle from 0° to 180° every 10°. The example mesh for wind angle γ = 40° is shown in Figures 12 and 13.

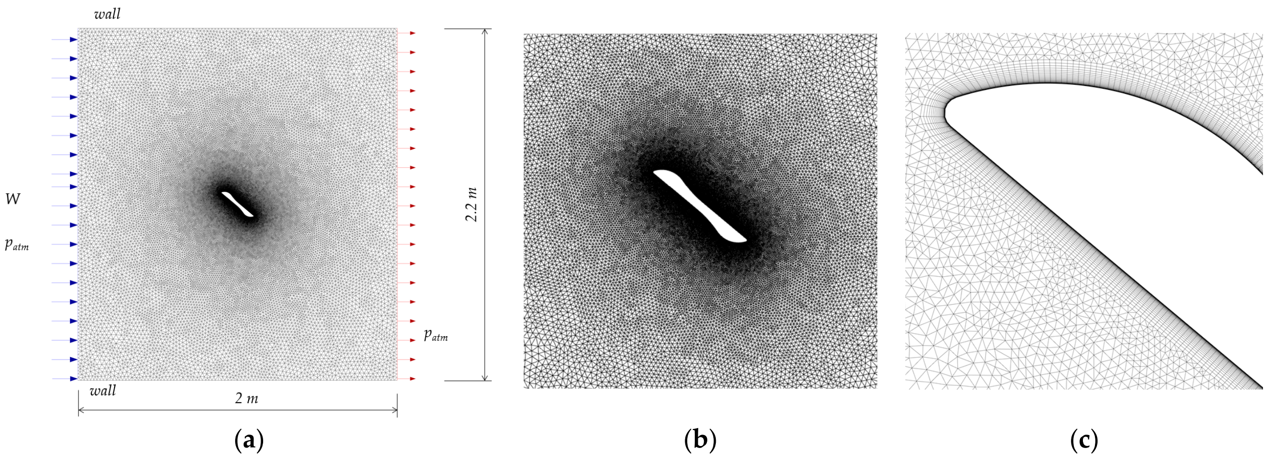

Figure 12. (**a**) Mesh and boundary conditions for the SC blade; (**b**) mesh refinement around the blade; (**c**) mesh for the boundary layer.

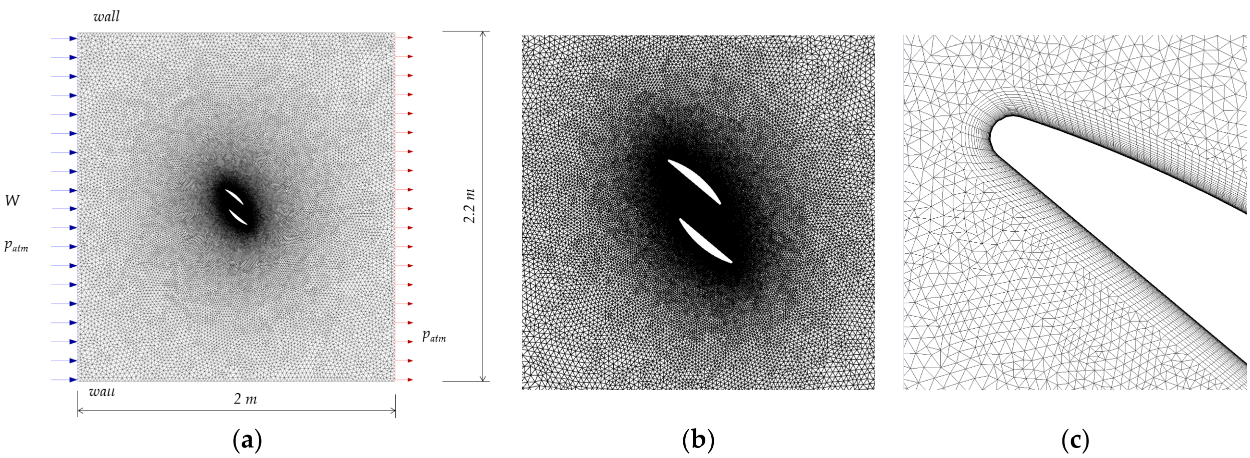

Figure 13. (**a**) Mesh and boundary conditions for the DC blade; (**b**) mesh refinement around the blade; (**c**) mesh for the boundary layer.

Irregular elements were used to generate discrete models, which size corresponded to the size of the measuring section in the wind tunnel. The mesh for a single problem was built from around 100,000 triangular elements in the regions of free flow and about 20,000 quad elements in the regions including the inflation layer near the blade surface. For the analyzed blade cross-section geometry and for the adopted wind angle range, separation of the boundary could have occurred. For that reason, the viscous sublayer near the blade's surface had to be resolve directly. It is obtained by accepting the nondimensional parameter referred to the boundary layer mesh y + = 1. However, when using ANSYS Fluent, the value of y + < 5 is still acceptable as long as it is within the viscous sublayer [40]. In this study, the condition of y + <1 was assumed, and it was obtained with inflation layer parameters and the CFD analyses assumptions listed below:

- Height of first layer = 0.01 mm;
- Layers number = 30;

- Growth rate = 1.15;
- The speed of the wind w = 12.5 m/s;
- Air density ρ = 1.16 kg/m^3;
- Air viscosity μ = 1.7894 × 10^{-5} kg/ms;
- Averaged Reynolds number Re = 1.7 × 10^6;
- Pressure-based solver used;
- Convergence of the numerical solution for mass and momentum residuals < 10^{-3}.

2.3.3. Mesh Validation

The validity of numerical analysis is usually tested by comparing numerical and experimental data. In turn, the convergence of the CFD solutions is examined by checking the mesh sensitivity. The mesh independence tests, based on mesh refinement, were conducted for the angle of the wind attack γ = 40° both for single coherent and dual coherent blades. The influence of the mesh density on the drag force P_x and the lift force P_y acting on the blades was verified. The effects of the mesh independence tests are presented in Figures 14 and 15 for single and dual coherent blades, respectively.

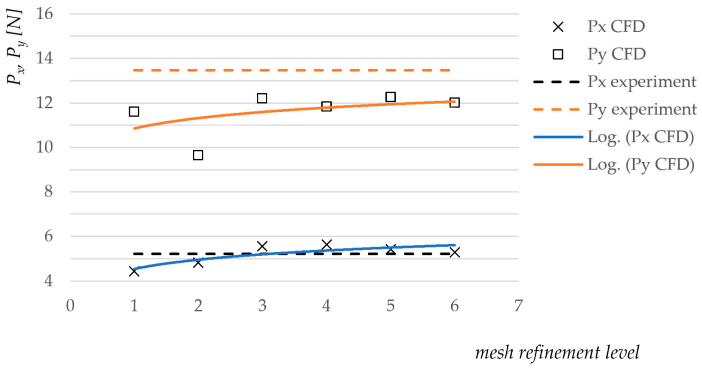

Figure 14. Mesh independence test results for the SC blade (γ = 40°).

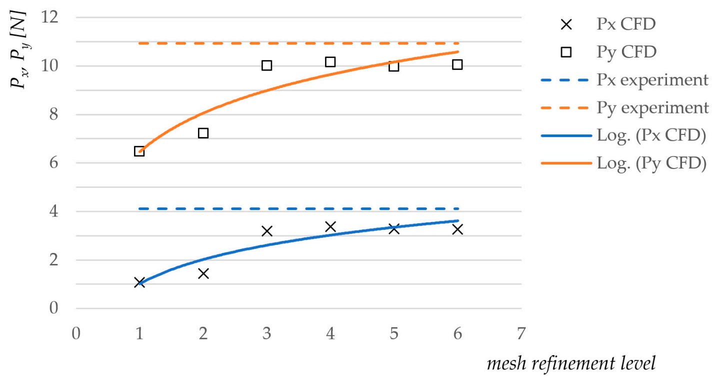

Figure 15. Mesh independence test results for the DC blade (γ = 40°).

The level 1 of mesh refinement indicated the coarse mesh. In turn, mesh refinement levels 2–6 represented rising levels of mesh compaction. Finally, level 5 was adopted for all computational cases. The corresponding mesh size was about 150,000 finite elements, depending on the wind direction.

3. Results and Discussion

The example results of CFD analysis both for the single coherent and the dual coherent blades are shown in Figures 16 and 17. The examples of velocity and pressure distributions are presented for the angle of the wind attack γ = 40° to illustrate and compare airflow around the single and dual coherent blades. The main visible difference in the velocity distributions is the effect of the gap between the blades in the dual coherent blade cross-section. The gap affects different speed distribution and pressure distribution.

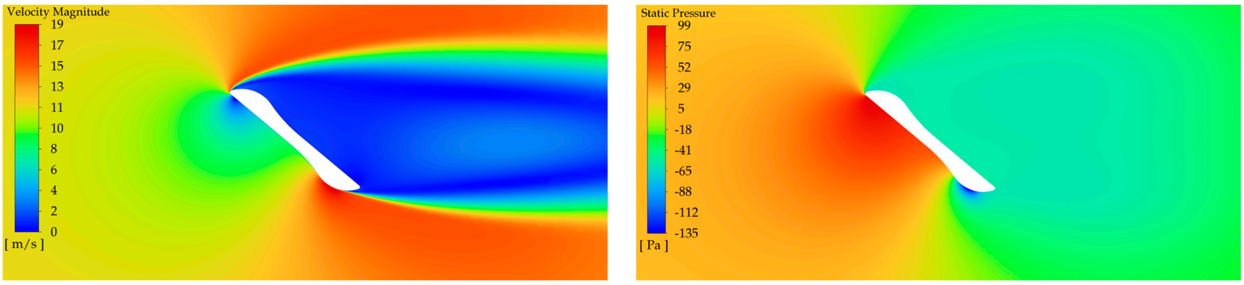

(**a**) (**b**)

Figure 16. Results of CFD analysis for the SC blade (γ = 40°): (**a**) distribution of velocity magnitude; (**b**) distribution of pressure.

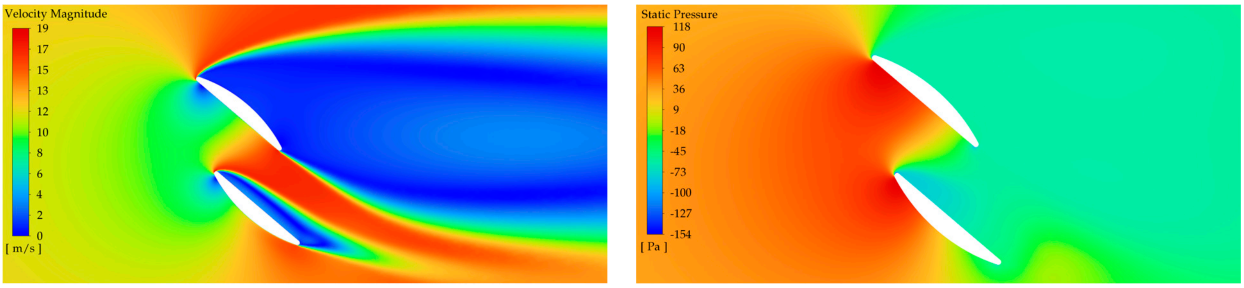

(**a**) (**b**)

Figure 17. Results of CFD analysis for the SC blade (γ = 40°): (**a**) distribution of velocity magnitude; (**b**) distribution of pressure.

Despite the locally visible higher pressure values for the dual coherent blade, no such significant aerodynamic effect was observed for any angle of the wind attack. In the case of the dual coherent blade, the effect of the wind creates mainly the drag force. In contrast, for the single coherent blade the significant aerodynamic effect caused by the lift force occurred in the range of the wind angle $\gamma = 0° \div 40°$. The differences in results for single and dual coherent blade cross-sections were discussed in detail by the analysis of forces and moments in the following paragraphs.

3.1. Comparison of Aerodynamic Loads Acting on the SC and DC Blades

Detailed results of the CFD simulations and experimental tests relating to the aerodynamic loads acting on the single blade of the wind rotor, with respect to the wind attack angle γ, are presented in Figures 18–20. Some differences between experimental and simulation data may result from simplifying assumptions made for the numerical analysis. These included the following: not considering surface condition in the finite element model, which can change the location of airflow separation, and consequently affect aerodynamic loads; adopting a 2D model for CFD calculations; assuming wind speed as an average value from the wind profile, and assuming average turbulence intensity, which can cause differences in the maximum aerodynamic forces.

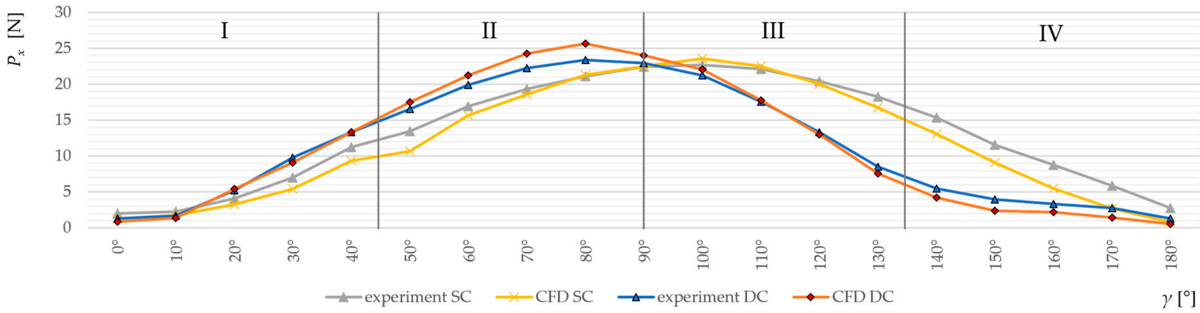

Figure 18. Drag force P_x depending on the angle of the wind attack γ.

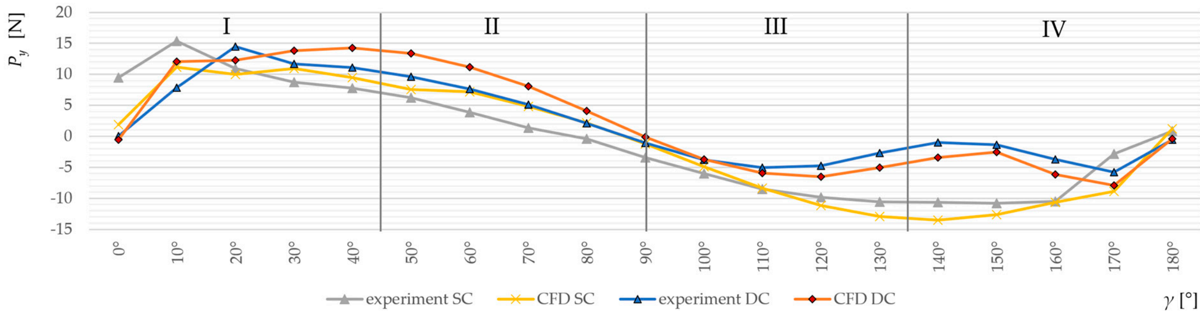

Figure 19. Lift force P_y depending on the angle of the wind attack γ.

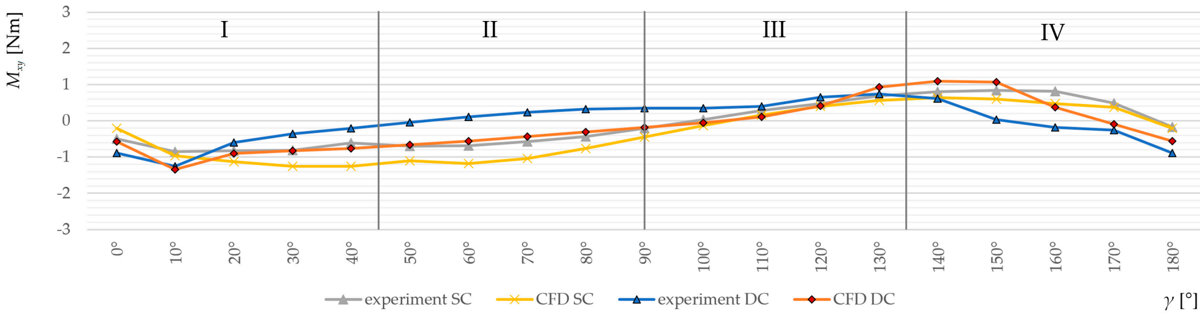

Figure 20. Aerodynamic torque M_{xy} depending on the angle of the wind attack γ.

Comparing the results of aerodynamic drag P_x, shown in Figure 18, it can be noticed that for the range of the wind attack angles γ = 0°÷90° (range I–II), the dual coherent blade generated significantly higher drag than the single coherent blade. The higher drag is advantageous for this angle range to obtain the higher propelling torque.

In turn, considering the wind attack angle γ = 90° ÷ 135° (range III), the drag obtained for DC blade was lower and therefore disadvantageous for that angle range compared to the drag obtained for SC blade, because the blade moved downwind. Concerning the wind attack angle γ = 135° ÷ 180° (range IV), the DC blade provided low and almost constant value of the drag, which was lower than 5 N. Low drag values in this range are preferred because the blade returns upwind to its starting position.

Comparing the results of the lift force P_y, shown in Figure 18, it can be noticed, that higher values occurred both for single and dual coherent blades, when considering the wind angles of attack γ = 0° ÷ 90° (range I–II). In accordance with the diagram presented in Figure 4a and related x, y coordinate system, higher values of the lift force P_y, for in the range I–II have a positive effect on increasing the propelling torque. Considering the values of the wind angles of attack γ = 90° ÷ 180° (range III–IV), lower P_y values in the range from 0 to around -7 N were obtained for the DC blade. In contrast for the SC blade, the values of the lift force P_y ranged from about −15 N to −10 N and had a better effect on increasing the starting torque. The effect of higher lift force P_y is advantageous for generating propelling torque, especially when the blade moves upwind, and the drag force does not occur.

The small values of aerodynamic torque M_{xy} were obtained throughout the whole I–IV range, as shown in Figure 20. Aerodynamic torque has a minor impact on the torque generated by the entire turbine. The main influence on the total propelling torque is caused by P_x and P_y aerodynamic forces. Aerodynamic torque M_{xy} is generated by airflow around the airfoils. Although the presence of aerodynamic torque is beneficial, its importance for the overall turbine performance is relatively low because the drag force effect dominates.

3.2. Example of Calculating the Propelling Torque

Based on the data obtained from experimental tests and CFD analysis, it was possible to calculate the starting torque of the carousel wind rotor. In accordance to Figure 11, the single blade was affected by aerodynamic drag P_x, lift force P_y, aerodynamic torque M_{xy} and by loads associated with the blade R_η, R_ξ and the torque $M_{\eta\xi}$ in movable coordinate system η, ξ associated with the blade. The associated forces and torques can be calculated using the following formulas:

$$R_\eta = P_x cos\left(\frac{\alpha}{2}\right) - P_y sin\left(\frac{\alpha}{2}\right) \tag{19}$$

$$R_\xi = P_x sin\left(\frac{\alpha}{2}\right) + P_y cos\left(\frac{\alpha}{2}\right) \tag{20}$$

$$M_{\eta\xi} = M_{xy} \tag{21}$$

The following assumptions were accepted for calculations: the rotor included three blades; the rotor radius R = 1.5 m; the wind angle $\gamma = \alpha/2$; the peripheral speed V_0 = 0, and the angle β = 0. In accordance with Figure 4a, the total propelling torque for one blade $M_1(\alpha_s)$, depending on the angle of the rotor rotation α(αs) is given by following equation:

$$M_1(\alpha_s) = \left[-R_\eta \cdot cos\left(\frac{\alpha}{2}\right) + R_\xi \cdot sin\left(\frac{\alpha}{2}\right)\right] \cdot R + M_{\eta\xi} \tag{22}$$

The resultant torque for all rotor blades $M_{\mathrm{III}}(\alpha_s)$ related with η, ξ coordinates is the sum of the torques for three rotor blades $M_1(\alpha_s)$, $M_2(\alpha_s)$, and $M_3(\alpha_s)$ as a function of the rotor rotation angle α(αs). The total torque for all rotor blades can be written as follows:

$$M_{III}(\alpha_s) = M_1(\alpha_s) + M_2(\alpha_s) + M_3(\alpha_s) \tag{23}$$

The calculations were conducted using data obtained from experiments. The obtained rotor torque values can be used to estimate the maximum rotor peripheral speed, which will no longer increase with the increasing wind speed. The total propelling torque depending on the position of the blade is presented in Figure 21a,b both for the single and dual coherent blades. Since the carousel wind rotor is equipped with self-adjusting system, the blades reach positions A1 for 0° and A7 for 180° in accordance with Figure 4a.

The average total torque $M_{\mathrm{III}}(\alpha_s)$ for the rotor with three single coherent blades was equal to was 43.7 Nm. In turn for the rotor with three DC blades it reached the value of 41.3 Nm. Comparing these average values, it was concluded that the rotor with single coherent blades generated 5.5% higher total propelling torque. However, it should be noted that despite the higher average total torque for the rotor with SC blades, there were locally larger deviations from the average value of total torque. This means that this rotor operated less smoothly than the rotor with dual coherent blades. The maximum value of total propelling torque was 47.8 Nm for the rotor with SC blades and 44.6 Nm for the rotor with DC blades, which was 6.7% less.

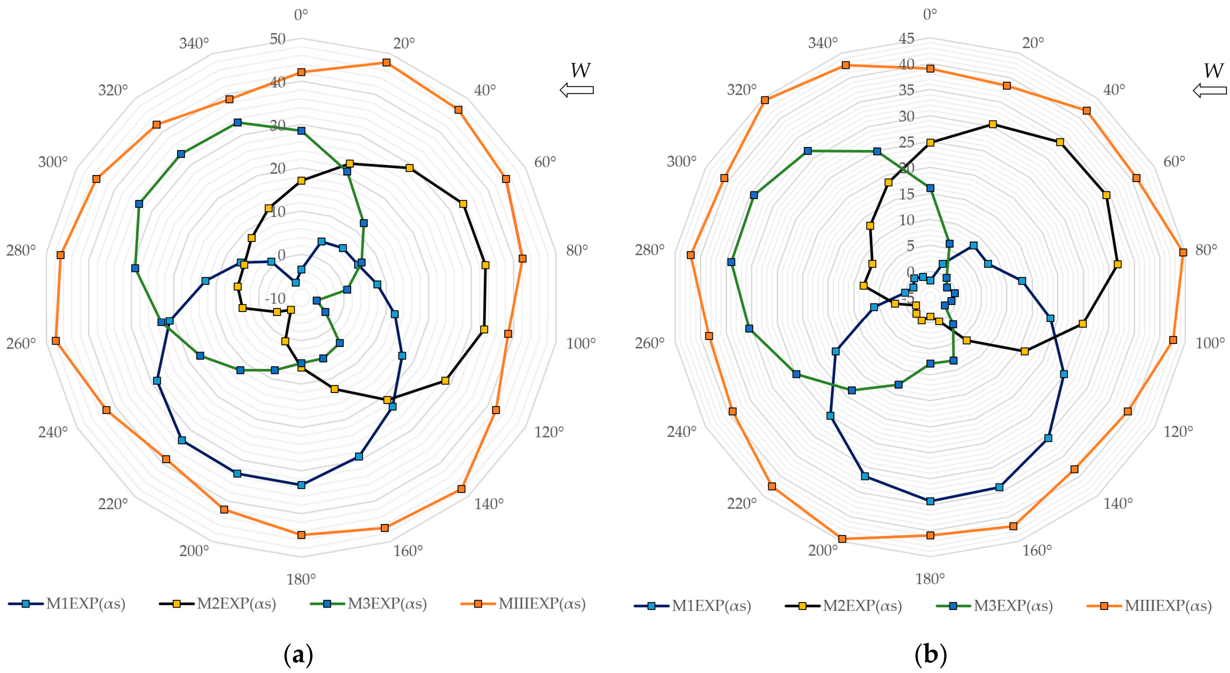

Figure 21. The propelling torque for the wind direction W depending on the blade position $\alpha(\alpha s)$ for: (**a**) the SC blade; (**b**) the DC blade.

In addition, for the rotor with SC blades, higher torque values were obtained for the ranges of $\alpha(\alpha s)$: 20–80°, 140–200° and 260–320°, and mainly the lift force was generated. In contrast, for the rotor with DC blades, higher torque values were obtained for the ranges of $\alpha(\alpha s)$: 80–100°, 200–220° and 320–340°, and the drag force was dominated. An analogous analysis can be performed for turbines with various numbers of blades.

4. Conclusions

Two types of blades were compared for the application in the vertical axis carousel wind rotor. These were blades with the single and dual coherent cross-sections. Real-scale physical models of both blades type were made and experimentally tested in the aerodynamic wind tunnel. To validate the results, at the same time, two-dimensional discrete models of blades cross-sections were prepared. The CFD numerical analysis was then performed considering the same cases and boundary conditions that were accepted in experiments.

The obtained results of aerodynamic forces and aerodynamic torques were first compared by considering a single blade. Based on the obtained results, it was concluded, that the dual coherent blade provided more advantageous, higher aerodynamic drag P_x when moving downwind, and also more advantageous, lower lift force P_y when moving upwind. The aerodynamic torque M_{xy} was also concluded to have a minor effect on the total torque, which was generated by the aerodynamic forces acting on the corresponding rotor radii.

However, the design of a vertical axis carousel wind rotor assumes that there are at least three identical blades in the system. Therefore, in the last step of the comparison, the total starting torque $M_{III}(\alpha_s)$ was calculated for the example of the vertical axis carousel wind rotors with three SC and DC blades in the system.

It was concluded, that for the above configurations, the rotor with three SC blades can generate slightly higher maximum starting torque than the rotor with three DC blades, but at the same time, a greater variation of starting torque as a function of wind angle is observed for SC blades. The rotor with three DC blades involved mainly the drag force in contrast to the rotor with three SC blades, which also involved the lift force to a greater extent. Despite the rotor with DC blades obtained greater values of the drag forces on the blades, the rotor with SC blades obtained a greater starting torque.

The obtained results can be useful in designing vertical axis carrousel wind rotors with self-adjusting system. The findings presented in the article may be particularly useful in related research aimed at optimizing the shape of vertical axis wind turbine blades. Further research on designing and comparing blade geometries dedicated to a vertical axis carousel wind rotor will address the optimization of cross-sectional dimensions to achieve higher and more uniform total torque as a function of the number of rotor blades.

Author Contributions: Conceptualization, M.A. and F.L.; methodology, M.A. and F.L.; software, F.L.; validation, M.A. and F.L.; formal analysis, M.A.; investigation, M.A.; data curation, M.A. and F.L.; writing—original draft preparation, M.A. and F.L.; writing—review and editing, M.A. and F.L.; visualization, M.A. and F.L.; supervision, M.A.; All authors have read and agreed to the published version of the manuscript.

Funding: This research received no external funding.

Institutional Review Board Statement: Not applicable.

Informed Consent Statement: Not applicable.

Data Availability Statement: Data is contained within the article.

Conflicts of Interest: The authors declare no conflict of interest.

References

1. BP Statistical Review of World Energy, 2022, 71st Edition. Available online: https://www.bp.com/content/dam/bp/business-sites/en/global/corporate/pdfs/energy-economics/statistical-review/bp-stats-review-2022-full-report.pdf (accessed on 19 October 2023).
2. Bošnjaković, M.; Katinić, M.; Santa, R.; Marić, D. Wind Turbine Technology Trends. *Appl. Sci.* **2022**, *12*, 8653. [CrossRef]
3. Kamran, M. *Fundamentals of Smart Grid Systems*; Chapter 6-Planning and modeling of wind energy systems; Academic Press: Los Angeles, CA, USA, 2022.
4. Wang, Q.; Huang, P.; Gan, D.; Wang, J. Integrated Design of Aerodynamic Performance and Structural Characteristics for Medium Thickness Wind Turbine Airfoil. *Appl. Sci.* **2019**, *9*, 5243. [CrossRef]
5. Jaramillo-Cardona, J.; Perafan Lopez, J.; Torres-Madroñero, J.; Nieto-Londoño, C.; Sierra-Perez, J. Techno-economic assessment of small wind turbines under la Guajira-Colombia resource conditions. *CTF-Cienc. Tecnol. Y Futuro.* **2022**, *12*, 45–56. [CrossRef]
6. Whittlesey, R. *Wind Energy Engineering*; Chapter 10-Vertical Axis Wind Turbines: Farm and Turbine Design; Academic Press: Los Angeles, CA, USA, 2017.
7. Senga, H.; Umemoto, H.; Akimoto, H. Verification of Tilt Effect on the Performance and Wake of a Vertical Axis Wind Turbine by Lifting Line Theory Simulation. *Energies* **2022**, *15*, 6939. [CrossRef]
8. Aslam Bhutta, M.M.; Hayat, N.; Farooq, A.U.; Ali, Z.; Jamil, S.R.; Hussain, Z. Vertical axis wind turbine-A review of various configurations and design techniques. *Renew. Sustain. Energy Rev.* **2012**, *16*, 1926–1939. [CrossRef]
9. Wilberforce, T.; Olabi, A.G.; Sayed, E.T.; Alalmi, A.H.; Abdelkareem, M.A. Wind turbine concepts for domestic wind power generation at low wind quality sites. *J. Clean. Prod.* **2023**, *394*, 136137. [CrossRef]
10. Apelfröjd, S.; Eriksson, S.; Bernhoff, H. A Review of Research on Large Scale Modern Vertical Axis Wind Turbines at Uppsala University. *Energies* **2016**, *9*, 570. [CrossRef]
11. Kumar, R.; Raahemifar, K.; Fung, A.S. A critical review of vertical axis wind turbines for urban applications. *Renew. Sustain. Energy Rev.* **2018**, *89*, 281–291. [CrossRef]
12. Tjiu, W.; Marnoto, T.; Mat, S.; Ruslan, M.H.; Sopian, K. Darrieus vertical axis wind turbine for power generation II: Challenges in HAWT and the opportunity of multi-megawatt Darrieus VAWT development. *Renew. Energy* **2015**, *75*, 560–571. [CrossRef]
13. Yang Il Yoon, Vertical Shaft Type Darius Windmill. US Patent 2011/0042962 A1, 24 February 2011.
14. Tian, W.; Ni, X.; Li, B.; Yang, G.; Mao, Z. Improving the efficiency of Darrieus turbines through a gear-like turbine layout. *Energy* **2023**, *267*, 126580. [CrossRef]
15. Gorelov, D.N. Energy characteristics of Darrieus rotor (review). *Thermophys. Aeromech.* **2010**, *17*, 301–308. [CrossRef]
16. Islam, M.; Ting, D.S.K.; Fartaj, A. Aerodynamic models for Darrieus-type straight-bladed vertical axis wind turbines. *Renew. Sustain. Energy Rev.* **2008**, *12*, 1087–1109. [CrossRef]
17. Gharib-Yosry, A.; Blanco-Marigorta, E.; Fernández-Jiménez, A.; Espina-Valdés, R.; Álvarez-Álvarez, E. Wind-Water Experimental Analysis of Small SC-Darrieus Turbine: An Approach for Energy Production in Urban Systems. *Sustainability* **2021**, *13*, 5256. [CrossRef]
18. Maican, E.; Dumitrescu, L.; Rădoi, R.; Ciobanu, O.; Preda, D. Analysis and optimization of a savoniusdarrieus hybrid wind turbine. *Int. J. Eng.* **2021**, *19*, 151–156.
19. Mohan Kumar, P.; Surya, M.R.; Sivalingam, K.; Lim, T.-C.; Ramakrishna, S.; Wei, H. Computational Optimization of Adaptive Hybrid Darrieus Turbine: Part 1. *Fluids* **2019**, *4*, 90. [CrossRef]

20. Savonius, S.J. The S-rotor and its applications. *Mech Eng.* **1931**, *53*, 333–338.
21. Kamoji, M.A.; Kedare, S.B.; Prabhu, S.V. Experimental investigations on single stage modified Savonius rotor. *Appl. Energy* **2009**, *86*, 1064–1073. [CrossRef]
22. Moutsoglou, A.; Yan, W. Performance Tests of a Benesh Wind Turbine Rotor and a Savonius Rotor. *Wind. Eng.* **1995**, *19*, 349–362.
23. Van Bussel, G.; Mertens, S.; Polinder, H.; Sidler, H.F.A. The Development of Turby, a Small VAWT for the Built Environment. In Proceedings of the Global Windpower 2004 Conference, Chicago, IL, USA, 28–31 March 2004.
24. Zhang, H.; Li, Z.; Xin, D.; Zhan, J. Improvement of Aerodynamic Performance of Savonius Wind Rotor Using Straight-Arc Curtain. *Appl. Sci.* **2020**, *10*, 7216. [CrossRef]
25. Rogowski, K. CFD Computation of the H-Darrieus Wind Turbine—The Impact of the Rotating Shaft on the Rotor Performance. *Energies* **2019**, *12*, 2506. [CrossRef]
26. Cheng, Q.; Liu, X.; Ji, H.S.; Kim, K.C.; Yang, B. Aerodynamic Analysis of a Helical Vertical Axis Wind Turbine. *Energies* **2017**, *10*, 575. [CrossRef]
27. Ryś, J. 1993 Arrangement for Self-Positioning a Wing Motor in Wind's Eye Position. Patent PAT.170515, 13 May 1993.
28. Wind Engineering Laboratory. Available online: http://www.windlab.pl/en/ (accessed on 19 October 2023).
29. *EN 1991-1-4*; Eurocode 1: Actions on Structures-Part 1–4: General Actions–Wind Actions. European Committee for Standardization: Brussels, BE, USA, 2005.
30. Continuity and Momentum Equations. In Ansys Fluent Theory Guide. Available online: https://www.afs.enea.it/project/neptunius/docs/fluent/html/th/node11.htm (accessed on 19 October 2023).
31. Menter, F.R. Zonal Two Equation k-ω Turbulence Models for Aerodynamic Flows. In Proceedings of the 23rd Fluid Dynamics, Plasmadynamics, and Lasers Conference, Orlando, FL, USA, 6–9 July 1993.
32. Menter, F.R. Two-Equation Eddy-Viscosity Turbulence Models for Engineering Applications. *AIAA J.* **1994**, *32*, 1598–1605. [CrossRef]
33. Wilcox, D.C. Formulation of the k-omega Turbulence Model Revisited. *AIAA J.* **2008**, *46*, 2823–2838. [CrossRef]
34. Chien, K.-Y. Predictions of Channel and Boundary-Layer Flows with a Low-Reynolds-Number Turbulence Model. *AIAA J.* **1982**, *20*, 33–38. [CrossRef]
35. Shear-Stress Transport (SST) k–ω Model. In Ansys Fluent Theory Guide. Available online: https://www.afs.enea.it/project/neptunius/docs/fluent/html/th/node67.htm (accessed on 19 October 2023).
36. Carraro, M.; De Vanna, F.; Zweiri, F.; Benini, E.; Heidari, A.; Hadavinia, H. CFD Modeling of Wind Turbine Blades with Eroded Leading Edge. *Fluids* **2022**, *7*, 302. [CrossRef]
37. Meana-Fernández, A.; Fernández Oro, J.M.; Argüelles Díaz, K.M.; Galdo-Vega, M.; Velarde-Suárez, S. Application of Richardson extrapolation method to the CFD simulation of vertical-axis wind turbines and analysis of the flow field. *Eng. Appl. Comput. Fluid Mech.* **2019**, *13*, 359–376. [CrossRef]
38. Gantasala, S.; Tabatabaei, N.; Cervantes, M.; Aidanpää, J.-O. Numerical Investigation of the Aeroelastic Behavior of a Wind Turbine with Iced Blades. *Energies* **2019**, *12*, 2422. [CrossRef]
39. Ansys Fluent Theory Guide. Available online: https://www.afs.enea.it/project/neptunius/docs/fluent/html/th/node67.htm#turb-sec-komega-sst (accessed on 19 October 2023).
40. Ansys Fluent Theory Guide. Available online: https://www.afs.enea.it/project/neptunius/docs/fluent/html/th/node67.htm (accessed on 19 October 2023).